PHYSICAL REVIEW B, VOLUME 64, 125302

Electronic structure consequences of In/Ga composition variations in self-assembled $In_xGa_{1-x}As$/GaAs alloy quantum dots

J. Shumway, A. J. Williamson, and Alex Zunger
National Renewable Energy Laboratory, Golden, Colorado 80401

A. Passaseo, M. DeGiorgi, and R. Cingolani
Dipartimento Ingegneria dell'Innovazione, Università di Lecce, 73100 Lecce, Italy

M. Catalano
Insituto CNR-IME, c/o Dipartimento Ingegneria dell'Innovazione, Università di Lecce, 73100 Lecce, Italy

P. Crozier
Center for Solid State Science, Arizona State University, Tempe, Arizona 85287-1704
(Received 22 March 2001; published 5 September 2001)

Provided that the shape, size, and composition profile of semiconductor-embedded quantum dots are given, theory is able to accurately calculate the excitonic transitions, including the effects of inhomogeneous strain, alloy fluctuations, electron-hole binding, and multiband and intervalley coupling. While experiment can accurately provide the spectroscopic signature of the excitonic transitions, accurate determination of the size, shape, and composition profile of such dots is still difficult. We show how one can arrive at a consistent picture of both the material and the electronic structure by interactive iteration between theory and experiment. Using high-resolution transmission electron microscopy, electron-energy-loss spectroscopy, and photoluminescence (PL) spectroscopy in conjunction with atomistic empirical pseudopotential calculations, we establish a model consistent with both the observed material structure and measured electronic/optical properties of a quantum dot sample. The structural model with best agreement between measured and predicted PL is a truncated cone with height 35 Å, base diameter 200 Å, and top diameter 160 Å, having a nonuniform, peaked composition profile with average 60% In content. Next, we use our best structure to study the effect of varying (i) the amount of In in the dots, and (ii) the spatial distribution of In within the dots. We find that by either increasing the amount of In within the dot or by concentrating a given amount of In near the center of the dot, both electrons and holes become more strongly bound to the dot. A small change of In content from 50 to 60% causes an exciton redshift of about 70 meV. Changing the composition profile from a uniform In distribution to a centrally peaked distribution can redshift the exciton by an additional 20–40 meV.

DOI: 10.1103/PhysRevB.64.125302 PACS number(s): 78.66.−w, 85.35.Be

I. INTRODUCTION

A. Interdependence of theory and experiment in determining the material and electronic structure of dots

Correct prediction of the excitonic gap of a semiconductor-embedded "self-assembled" quantum dot (QD) is highly nontrivial, yet it is a crucial prerequisite for understanding the basic optical properties of such systems. Even if the size, shape, and composition profile were know exactly, an appropriate theory must take into account (i) the existence of strong multiband coupling (e.g., electron-hole, hole-hole) without which the orbital symmetry, polarization ratio, and level splitting pattern can be qualitatively incorrect,[1–3] (ii) the existence of inhomogeneous and possibly anharmonic strain that not only varies strongly from the base to the top of the dot, but also has a lower point-group symmetry than that gleaned from the geometric shape of the dot,[4] (iii) multivalley (e.g., $\Gamma-X$) interactions[5,6] that may localize wave functions at the interface, (iv) the presence of significantly screened and size-dependent direct and exchange Coulomb interactions that shift the excitonic gap,[7,8] and (v) the possibility that the dot and its wetting layer (WL) are a random alloy rather than a pure phase,[9–13] with a possibly nonuniform composition profile,[14–16] necessitating a correct description of alloy statistical fluctuations.[17,18] Pseudopotential models of such quantum dots[1,2,19–21] are capable of taking these effects into account by retaining the atomistic nature of the system. These models use fast "order N" diagonalization of the pseudopotential Hamiltonian,[2,22] and are an alternative to the commonly used effective-mass[23–30] and $\mathbf{k}\cdot\mathbf{p}$[32–35] envelope-function approximations.

It has been possible in the past to fit the excitonic gap via models that neglect all, or most, physical factors indicated above.[24,25,27] Indeed, even single-band effective-mass treatments without explicit strain effects have successfully adjusted the geometric and other physical parameters of the dot to fit the measured gap.[24,25,27] However, it is now known that for a *given* size, shape, and composition of a self-assembled dot, simple theoretical models such as single-band effective mass produce significant errors in the excitonic gap and level spacings relative to more complete theoretical models using identical input parameters.[36] For example, assuming a pyramidal InAs dot with a base of 113 Å and height of 56 Å embedded in GaAs, and comparing to a pseudopotential treatment of the same Hamiltonian,[36] a single-band effective-

 ©2001 The American Physical Society

mass model overestimates the excitonic band gap by ~150 meV, misses all but 4 meV of the ~25 meV splitting in the second (p-like) electron level, and overestimates the splitting between first and second levels by ~80 meV. This is the case even if the effective-mass value is adjusted to take strain into account (otherwise errors are far larger). Eight-band $\mathbf{k}\cdot\mathbf{p}$ models do much better, e.g., the error in the excitonic gap is reduced to ~90 meV, although the splitting in the second electron level is still only ~3 meV (instead of 25 meV), and the spacings in the hole levels are too large.[36]

While a reliable theoretical description of self-assembled dots with *given* size, shape, and composition is now feasible, an accurate experimental determination of such geometric and compositional parameters needed as input to the calculations has proven to be difficult. Consequently, the interplay between theoretical methods and experimental growth and measurement techniques has become crucial to the understanding and engineering of dot properties. A central issue here is the need to know the compositional profile of the dot, discussed next.

B. The problem of compositional changes in dots

The composition profile of nominally $In_xGa_{1-x}As$ quantum dots grown on a GaAs substrate is not necessarily a uniform distribution of $In_xGa_{1-x}As$ alloy. Rather, the composition profile may depend on many aspects of the growth process, including (i) the nominal composition of the dot layer, (ii) the growth temperature,[11] (iii) strain-driven In enrichment of the dots,[14–16] (iv) composition changes during capping,[37] and (v) post-growth annealing.[9,10,38–41] Intermixing processes fall into two categories: (i) those that dilute the average In concentration of the dots, [leading to blue-shifted photoluminescence (PL)]; and (ii) those that enrich the In content in the core of the dot (leading to redshifted PL).

(i) *In-diluting compositional changes.* Growth temperature and annealing play a key role in composition lowering the In content of self-assembled dots. For example, post-growth thermal annealing of quantum dot samples blue shifts the PL emission of an ensemble of dots and narrows the linewidths of the inhomogeneously broadened PL peaks.[9,10,38–41] Indeed, nominally $In_{0.5}Ga_{0.5}As$ samples annealed for 30 s at 950 °C have been reported to have a blue shift of the first PL peak from 1.17 to 1.35 eV, with an accompanying line narrowing from 61 to 24 meV.[9] Using high-resolution cross-sectional scanning tunneling microscopy (STM), Lita *et al.*[42] observed the vertical distribution of In atoms in annealed samples. They find both vertical interdiffusion of In out of the dot with a diffusion length of 1.25 nm as well as an exponentially decaying In-rich tail above the dots, attributed to surface segregation. Even in unannealed samples, growth temperatures above 420 °C have been observed to cause significant Ga incorporation into nominally InAs dots.[11] STM measurements of the volume of uncapped dots have shown that growth of nominally InAs dots at a typical temperature of ≈500 °C actually produces alloy dots with 30% Ga content.[11] Large Ga content in nominally InAs dots has also been observed with grazing incident x-ray diffraction.[12,13]

(ii) *In-enriching compositional changes.* A competing composition changing effect has recently been reported: the In-enrichment of InGaAs/GaAs alloy dots.[14–16] Both plan-view transmission electron microscopy (TEM)[14] and x-ray diffraction[15] have indicated a higher average In content in the quantum dot compared to either the nominal composition or the measured wetting layer composition. Liu *et al.*[16] have measured the composition profile of large dots (450 Å base and 100 Å height) in [110] cross-section STM images, and find an In rich core with an inverted-triangular shape. They have suggested that the In-enrichment and inverted-triangular profile is due to the strain profile of the dot attracting In nonuniformly during the growth process. Grazing incidence x-ray measurements on uncapped nominally InAs dots confirm an In content that increases from bottom to top, but with a laterally uniform profile, rather than an inverted-triangular distribution.[12,13] Fry *et al.*[30] have observed an electric dipole attributed to the center of gravity of the hole being above that of the electron,[30] and a similar dipole has been seen in other quantum dots samples.[31] Effective-mass[23,30] and pseudopotential[21] calculations have confirmed that such a dipole moment is consistent with a graded indium composition, with indium content increasing from the bottom to the top of the dot.[21,23]

The blue shifting of PL lines due to In/Ga composition changes has been studied theoretically within the effective-mass approximation (EMA) for quantum wells[43] and lens-shaped dots.[44] In the calculations, the composition profile of the barriers was diffused, changing abrupt interfaces into graded interfaces, and both the effective mass and confining potential were made material dependent. Our calculations differ from these previous calculations in two significant ways: (i) the compositional variation is treated with pseudopotential Hamiltonian for atomistic random alloy, which correctly describes alloy optical bowing and statistical fluctuations; and (ii) our composition profile, taken from energy dispersive x-ray (EDX) and electron-energy-loss spectroscopy (EELS) measurements, has a peaked rather than broadened In distribution. The extent to which such composition changes, modeled atomistically, lead to a simple change in confining potential will be discussed in Sec. V B.

C. Outline of our present work

In this paper we report how experimental and theoretical tools have been used interactively to determine the geometric and compositional parameters and the resulting electronic properties of InGaAs/GaAs self-assembled alloy quantum dots, grown by metal-organic chemical vapor deposition (MOCVD) with nominal 50% In content and a deposition of four monolayers (ML's). A previous paper[21] addressed InAs/GaAs dots made of nominally pure InAs, as opposed to the alloy dots studied here.

The logic sequence of our work is as follows. First, using TEM, EDX, and EELS, the structure of MOCVD-grown InGaAs/GaAs alloy quantum dots was determined, leading to the structural and compositional parameters depicted as "Model 1" in Fig. 1(a). Second, pseudopotential calculations of this structure were carried out, considering both a uniform

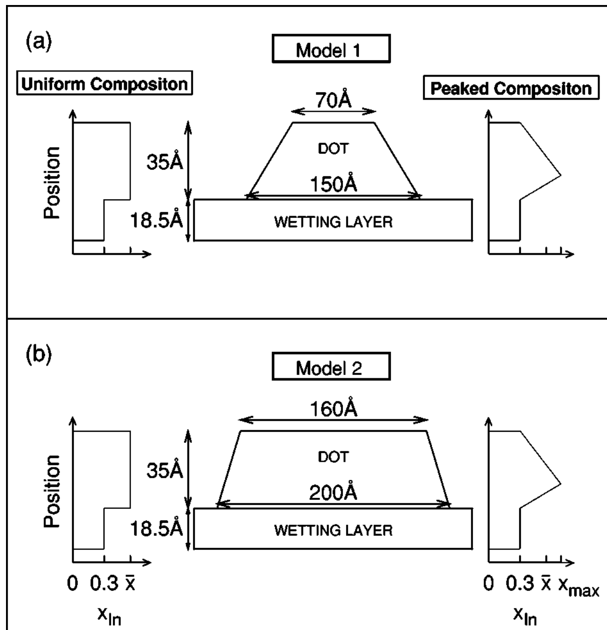

FIG. 1. Schematic representation of the two structural models used in this work, with size and shapes based on TEM and EELS images. (a) Model 1 is our first model, and (b) Model 2 our revised model, based on higher quality measurements. The In distribution for the uniform and nonuniform, peaked composition profiles are shown on the sides of the figure.

In composition profile and a nonuniform, peaked profile (as shown on the left and right sides of Fig. 1) and covering a range of possible In composition values. Comparison of the excitonic energies with those measured via photoluminescence led to a discrepancy of 100–150 meV for the fundamental exciton, and 70–110 meV for the second exciton. Most importantly, this structural model led to the existence of only a single, dot-localized electron level (the higher levels being wetting-layer like), while the observed PL consists of a few peaks. Third, subsequent high-resolution TEM measurements were carried out, leading to a different structural model depicted as "Model 2" in Fig. 1(b). Here the base diameter changed from 150 to 200 Å and the top diameter changed from 70 to 160 Å. Fourth, the pseudopotential technique was applied to the "Model 2" structure. The discrepancy between the calculated and measured excitonic transition is now reduced to $\sim$30 and $\sim$10 meV for the first and second excitons, and the calculated wetting layer transition is within 10 meV of experiment. Most importantly, this structural model produces six dot-localized electron states, grouped into three energy shells, in agreement with the observed PL. We conclude that the dot has a nonuniform, peaked composition profile with average In content of 60%. This iterative experiment-theory interaction highlights the sensitivity of the electronic structure to the material structure and the importance of accurate measurements of the latter. Finally, having established a reasonable size and composition profile, we use our pseudopotential technique to investigate in detail the electronic structure and wave functions of this dot, as well as to study the generic effect of composition variations on the properties of such dots.

II. EXPERIMENTAL TECHNIQUES

Transmission electron microscopy is a suitable technique for the characterization of low-dimensional materials at nanoscales, due to its high spatial resolution and the possibility of combining structural and analytic techniques. In the present work, we combine high-resolution transmission electron microscopy (HRTEM) observations with EDX and EELS to study the structural and chemical features of the InGaAs/GaAs alloy quantum dots. The assessment of the quantum dot shape and size was performed by HRTEM and corroborated by the comparison with plan-view electron microscopy images, atomic force microscopy (AFM), and scanning tunneling microscopy (STM).[45] The spatially resolved composition profile was measured by high spatial resolution EDX and EELS.

The samples were grown by a horizontal low-pressure Aixtron reactor at 550 °C, using standard precursors for InGaAs and GaAs. The base pressure was 20 mbar, and the III/V ratio was fixed around 100 with a deposition rate of 1 ML/sec. $[0\bar{1}1]$ cross-sectional specimens were prepared for TEM studies by mechanical polishing down to a thickness of less than 10 μm, then the thickness was further reduced to electron transparency with a 4-kV Ar^{++} ion mill, using a GATAN Precision Ion Polishing System (PIPS). A JEOL 4000 EX II operating at 400 kV accelerating voltage with an interpretable resolution of 0.17 nm was used for the TEM observations. High spatial resolution chemical analysis was performed using a Vacuum Generator's HB501 scanning transmission electron microscope (STEM) equipped with a cold field emission gun, a windowless EDX spectrometer, and a GATAN parallel electron-energy-loss spectrometer (PEELS) with energy resolution better than 1 eV. The microscope is capable of focusing an intense electron beam to subnanometer dimensions. An EMISCAN data acquisition system is interfaced to the microscope both for digital image and spectral acquisition. The EMISCAN system can also be used to collect and process position resolved lines for EDX and EELS spectra with nanometer resolution.

The EDX and EELS measurements provide information about the relative In/As concentration ratio along the line scan direction, with a spatial resolution of the order of the probe size. However, the absolute calibration of the In content is not known at present, as it requires the precise knowledge of (i) beam/profile convolution effects, (ii) damage during preparation of the thin cross sections, and (iii) the overlap between the quantum dot and the surrounding matrix when the structure is viewed in projection. In order to have a simple and reliable calibration of the absolute In content, we scan a range of compositions for the wetting layer, calculate for each the exciton gap using the present pseudopotential method, and fit the gap to the observed PL measurements (note[46] that single-band models[45] produce different results than the multiband pseudopotential methods). In a PL experiment we probe some 100 square microns, i.e., a very large WL area with some dots on top. We assume that WL emission will reflect the ground level energy far from the dots. Atomistic pseudopotential calculations of a 4-ML $In_{0.5}Ga_{0.5}As$ WL yield a structure 12.1 Å thick with a

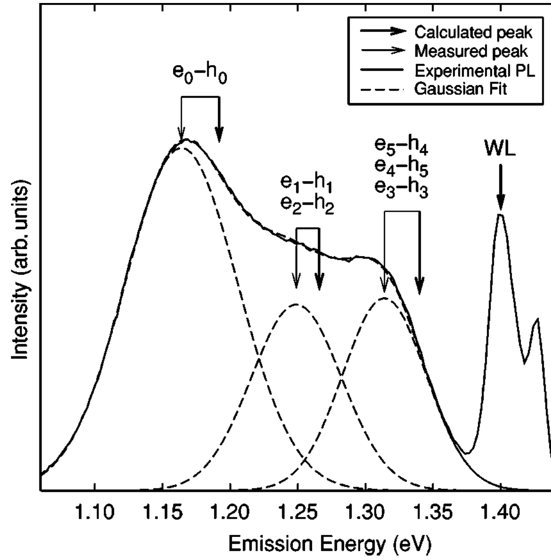

FIG. 2. Comparison of theoretical exciton energies (bold arrows) for Model 2 (and nonuniform, peaked In distribution with $\bar{x}_{\mathrm{In}}=60\%$) with experimental photoluminescence data (solid line). The PL between 1.1 and 1.37 eV is fit with three Gaussians (dashed lines) centered at 1.165, 1.250, and 1.315 eV (thin arrows). We attribute these to excitonic recombination from the first shell (e_0-h_0), second shell (e_1-h_1, e_2-h_2), and third shell ($e_3-h_3, e_4-h_5, e_5-h_4$), respectively. We attribute the double PL peak near 1.4 eV to emmision from the wetting layer.

1.40-eV excitonic gap, in excellent agreement with the observed PL peak at 1.4 eV, as well as the actual WL thickness from TEM. We therefore scale the In/As profiles determined by EDX and EELS so that the maximum of the In/As counts measured in the WL region corresponds to $x_{\mathrm{In}}=50\%$, and obtain the absolute composition profile of the nanostructures.

The measured PL spectra is shown as a solid line in Fig. 2. There are three prominent features in the PL spectra: (i) a broad peak centered around 1.17 eV, (ii) a second broad peak centered around 1.31 eV, and (iii) a double peak with energies 1.4 and 1.43 eV. Closer analysis of the two broad peaks at 1.17 and 1.31 eV reveals the possibility that these are actually three peaks. In fact, the PL spectra for energies between 1.0 and 1.35 eV is fit very well by three Gaussians centered at 1.165, 1.250, and 1.315 eV (shown by dashed lines in Fig. 2). These are summarized in the last column of Table I.

III. THEORETICAL TOOL: THE DIRECT-DIAGONALIZATION PSEUDOPOTENTIAL METHOD FOR QUANTUM DOTS

We use a screened atomistic pseudopotential Hamiltonian to determine the electronic structure arising from a given atomistic description of a quantum dot. The calculations proceed in four steps: (i) assume a size, shape, and composition for the dot and compute the equilibrium atomic displacements, (ii) set up and solve the pseudopotential single-particle equations to obtain energy levels and wavefunctions, (iii) compute the interparticle direct and exchange screened Coulomb interactions, and (iv) calculate exciton energies and transition dipole matrix elements. Addition of correlation corrections done elsewhere[47,48] via the "configuration-interaction" (CI) method is not included here.

For the present application to alloy dots, we wish to emphasize that our pseudopotential approach explicitly treats the alloy with atomic detail. We do not use a virtual crystal approximation (VCA), in which the InGaAs alloy is approximated by virtual cation atoms. Rather, our model contains three species of atoms (In, Ga, and As), and InGaAs alloy regions are constructed by randomly placing In or Ga atoms on cation sites, with the In/Ga probability chosen to achieve the desired composition.

TABLE I. Exciton energies E_X (in meV) as defined in Eq. (5) for Model 1 and Model 2 geometries (see Fig. 1) with different average In composition $\bar{x}_{\mathrm{In}}$ for both uniform and peaked composition profiles. Experimental energies listed are for the center of three Gaussians fit to the PL spectra in Fig. 2. Direct coulomb contributions J to exciton binding energy and the maximum In composition $x_{\mathrm{In}}^{\mathrm{max}}$ for each model are also listed. Bold typeface indicates model and composition having closest agreement with experiment.

		Model 1		Model 2		Expt.
	$\bar{x}_{\mathrm{In}}$	Uniform	Peaked	Uniform	Peaked	PL
	50%	1341 (24)	1327 (26)	1282 (21)	1264 (22)	
e_0-h_0	55%	1321 (26)	1309 (27)	1256 (22)	1255 (23)	1165
	60%	1300 (27)	1286 (28)	1236 (23)	**1192 (24)**	
	50%			1340 (17)	1328 (17)	
e_1-h_1	55%	unbound		1320 (17)	1315 (17)	1250
	60%			1295 (17)	**1264 (18)**	
	50%			1344 (17)	1332 (17)	
e_2-h_2	55%	unbound		1324 (17)	1319 (17)	1250
	60%			1299 (17)	**1268 (18)**	
e_3-h_3	60%	unbound		1361 (13)	**1334 (15)**	1315
e_4-h_5	60%	unbound		1368 (14)	**1345 (16)**	1315
e_5-h_4	60%	unbound		1369 (14)	**1345 (16)**	1315

A. Computing the equilibrium atomic positions

We place the InGaAs/GaAs alloy dot and wetting layer inside a supercell containing GaAs with dimensions $339 \times 339 \times 339$ Å (that is, $60a \times 60a \times 60a$, where $a = 5.65$ Å for bulk GaAs) and apply periodic boundary conditions to the supercell. The cell has been chosen to be large enough that interactions between periodic images do not significantly affect the strain fields and electronic wave functions.

Instead of treating strain with harmonic continuum elasticity theory, as is commonly used for dislocation free heterostructures,[28,32] we treat strain with an atomistic valence force field (VFF) model.[4,21,49,50] VFF offers a couple of advantages over harmonic continuum elasticity theory: (i) VFF can capture anharmonic effects, which are important in InAs/GaAs systems with 7% lattice mismatch (see Ref. 51 for a comparison of formation energies as calculated by VFF and first principles), and (ii) unlike contiuum elasticity models that depict conical or lens-shaped dots as having cylindrical symmetry, VFF has the correct point-group symmetry (C_{2v}), arising from the underlying zinc-blende lattice.[4] Our implementation of the VFF includes bond stretching, bond-angle bending, and bond-length/bond-angle interaction terms, so that we have three force constants for each material, which are fit to reproduce the C_{11}, C_{12}, and C_{44} elastic constants of the material.[21] The equilibrium atomic positions are determined by minimizing VFF total energy using a conjugate gradients algorithm. The length of the supercell in the [001] direction must also be relaxed due to expansion of the epitaxially strained InGaAs wetting layer, while the in-plane dimensions are fixed to the lattice constant of the GaAs substrate.

B. Determination of single-particle eigenstates

Having determined the atomic positions, we use a pseudopotential Hamiltonian to model the electronic structure of the dots,

$$H = -\frac{1}{2}\nabla^2 + \sum_{\alpha,n} v_\alpha[\mathbf{r} - \mathbf{R}_{\alpha n}, \mathrm{Tr}(\epsilon_{\alpha n})] + v_\alpha^{(\mathrm{SO})}, \qquad (1)$$

where α runs over atom species (In, Ga, and As), and n indexes the atoms. The local part of the pseudopotential, v_α, includes dependence on the local hydrostatic strain[19] $\mathrm{Tr}(\epsilon)$ and has been fit to bulk properties, including band structures, experimental deformation potentials, experimental effective masses, first-principles calculations of the valence-band offsets of GaAs and InAs, and the alloy bowing parameter of the InGaAs band gap.[21] Spin orbit interactions are included[21] via a nonlocal potential $v_\alpha^{(\mathrm{SO})}$.[21]

We solve the Hamiltonian Eq. (1) for the band-edge eigenstates using the strained linear combination of bulk bands (SLCBB) method.[2] The SLCBB methods has two features: (i) Wave functions are expanded in a basis set chosen from the bulk Bloch orbitals of materials (and strains) characteristic of the inhomogeneous system being solved,

$$\psi(\mathbf{x}) = \sum_{n}^{N_B} \sum_{k}^{N_k} C_{n,k} \phi_{n,k}^0(\mathbf{x}), \qquad (2)$$

where n indexes a set of bulk bands from different materials in various strain states, and vectors k are chosen from physically important regions of the Brillouin zone, both Γ and off Γ. (In $\mathbf{k}\cdot\mathbf{p}$ only Γ states are used.) This allows a physically motivated basis to be chosen that is much smaller than a plane-wave expansion, and is independent of system size. For example, the calculations here use the bulk bands from three structures: unstrained GaAs, strained GaAs, and strained InAs. Using eight bands and all k points with $k \leqslant 0.11$ Å^{-1} ($k \leqslant 0.22$ Å in the growth direction) produces 27 933 basis functions for the 1.7 million atom system considered here. (ii) The effects of strain are incorporated into the basis set by distorting the Bloch orbitals and evaluating the Hamiltonian under the approximation of slowly varying stain.[2] This straining of the basis set is necessary to provide a good basis for solving the Hamiltonian Eq. (1), which explicitly includes the displacement of strained atoms and the strain dependence of the atomic pseudopotentials. The SLCBB method distinguishes itself from $\mathbf{k}\cdot\mathbf{p}$ by the retention of different Bloch orbitals $\phi_{n,k}$ for different materials, the inclusion of off-Γ states in the basis, and explicit dependence on strain.

C. Computation of direct and exchange Coulomb energies

Having obtained the single-particle wave functions $\{\psi_i\}$ for the SLCBB calculations, the effect of Coulomb interactions are described by the direct and exchange screened Coulomb matrix elements, J_{ij} and K_{ij}, between single-particle eigenstates ψ_i and ψ_j. These matrix elements are given by the direct Coulomb integral,

$$J_{ij} = \int \int \frac{|\psi_i(\mathbf{r_1})|^2 |\psi_\mathbf{j}(\mathbf{r_2})|^2}{\bar{\epsilon}|\mathbf{r_1} - \mathbf{r_2}|} d\mathbf{r_1} d\mathbf{r_2}, \qquad (3)$$

and the exchange Coulomb integral,

$$K_{ij} = \int \int \frac{\psi_i^*(\mathbf{r_1}) \psi_\mathbf{i}(\mathbf{r_2}) \psi_\mathbf{j}^*(\mathbf{r_1}) \psi_\mathbf{j}(\mathbf{r_2})}{\bar{\epsilon}|\mathbf{r_1} - \mathbf{r_2}|} d\mathbf{r_1} d\mathbf{r_2}. \qquad (4)$$

Here we have used the bulk dielectric constant for $In_{0.5}Ga_{0.5}As$, taken to be $\bar{\epsilon} = (\epsilon_{\infty,\mathrm{InAs}} + \epsilon_{\infty,\mathrm{GaAs}})/2 = 13.0$. The use of pseudopotential ψ wave functions having atomic detail is known to give smaller Coulomb energies and different size scaling for both direct and Coulomb energies as compared to the commonly used effective-mass wave functions.[7]

D. Determination of excitation energies and transition strengths

Due to strong confinement in the dot, the excitonic energy arising from electron state i and hole state j is well described by first-order perturbation theory,

$$E_X = (\varepsilon_{ei} - \varepsilon_{hj}) - J_{ei-hj} + K_{ei-hj}\delta_{S,0}, \qquad (5)$$

where $\delta_{S,0} = 1$ for triplet states and 0 for singlet states. The exchange term K here is inter-band electron-hole exchange, which is quite small (≈ 1 meV) and therefore omitted in

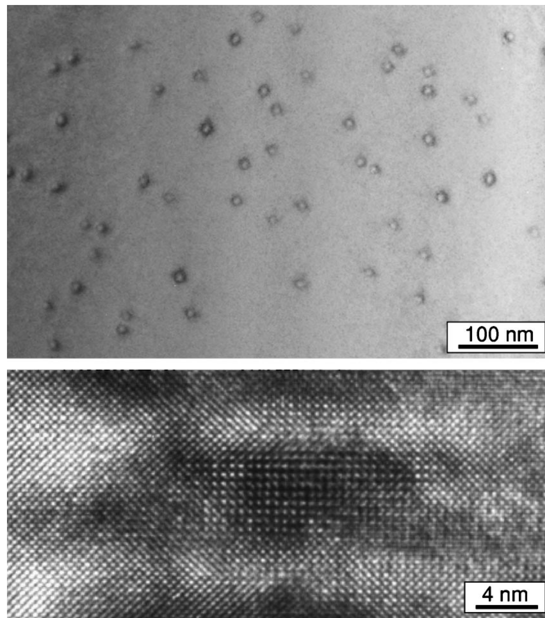

FIG. 3. TEM image of the dots in the [001] direction (top image) and the $[1\bar{1}0]$ direction (bottom image).

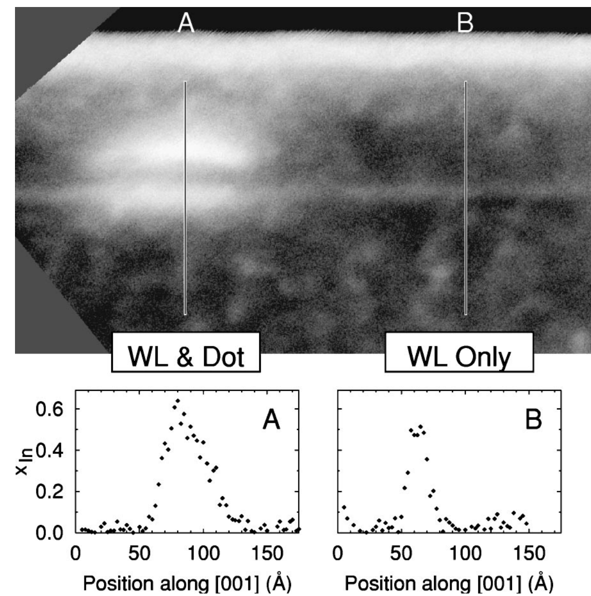

FIG. 4. STEM image in the $[1\bar{1}0]$ direction (top) and EELS scans (bottom graphs) showing the composition profile along the [001] direction. Line "A" goes up though the wetting layer and through the center of a dot, and line "B" goes up through the wetting layer far from the dot. The In content in the EELS data has been normalized to a 50% In composition in the wetting layer as determined by comparison between PL from the wetting layer and pseudopotential calculations.

this work. Note that these Coulomb energies are are evaluated from atomistic pseudopotential wave functions, not envelope functions.[7]

IV. INTERPLAY OF EXPERIMENT AND THEORY

A. First measurement of size and shape: Model 1

A first rough assessment of the dot shape and size was performed by a combination of atomic force microscopy (AFM) and TEM plan-view images. The former measurement was performed on uncapped quantum dots, showing the uniform dot base size distribution peaked around 150 Å, of height 35 Å. The capped samples were analyzed by TEM plan-view (see top of Fig. 3), showing a truncated pyramidal shape. The profile could not be determined very accurately by the plan view due to the complex image contrast, which is affected by strain, composition, and sample thickness. However, by combining the information obtained by the two methods we determined the structure to be a truncated conical shape, with a base diameter 150 Å, height 35 Å, and top diameter 70 Å.

Position resolved EDX and EELS experiments were performed by scanning a probe with a FWHM smaller than 1 nm both across several dots and across several regions on the wetting layer. The top portion of Fig. 4 is a STEM image of two dots. "A" and "B" mark respectively the lines where the scans were performed, corresponding to (*A*) a dot and (*B*) the wetting layer far from the dots. The strain contrast around the dot in the STEM image is evident. To check the concentration of In in the well and the dot we carried out position resolved EDX and EELS analysis.

The In/As concentration ratio derived from EELS is plotted as a function of position for the dot (graph "A" in Fig. 4) and the wetting layer (graph "B" in Fig. 4). The composition profiles derived from EDX (not shown) and EELS are consistent to within a few percent, indicating the excellent reproducibility of our measurements. The full width at half maximum (FWHM) of the WL profile is about 14 ± 3 Å. This is consistent with the real space TEM cross section and with the nominal growth parameters. Given the high spatial resolution of the experiment, the broadening of the composition profile indicates that the wetting layer has sharp interfaces with interdiffusion limited to about 1–2 ML's.

Unlike the case of the WL, the dot measurements show a considerable broadening and an asymmetry in the In composition profile. The measured In/As concentrations across the dot are usually higher than those obtained from the WL. The tail in the distribution is consistent with a somewhat tapered dot shape extending some 30–40 Å into the GaAs capping layer. Extraction of quantitative compositional In profiles from such projected experimental data is problematic. The energy-loss signal comes not only from the dot but also from the residual GaAs capping layers (which remain after cross sectioning) above and below the dot. The contribution from this capping layer becomes larger as the electron probe is scanned across the dot (away from the WL) thus, even if the In concentration in the dot is constant, the measured In/As ratio will decrease if the dot has tapered morphology. This problem is exacerbated because the structures of interest are comparable to the electron probe, resulting in In profiles which are broadened.

We have constructed Model 1, which is consistent with both the spectroscopic and morphological information obtained from the electron microscopy measurements. We assume that some In diffuses into the dot, resulting in a local

depletion of In from the wetting layer. We model the dot on a 6-ML wetting layer with a 30% In content [see Fig. 1(a)]. For simplicity we neglect the possibility of diffusion of In into the above capping layer. To study the effect of the In distribution, we have varied the In composition, using both a uniform profile and a nonuniform, peaked profile [shown on the left and right sides of Fig. 1(a)]. Based on the available data, we assume that the In concentration changes with height, using a piecewise linear function with a peaked maximum at one-third the dot height.

B. Pseudopotential calculations for Model 1 and comparison to experiment

To determine the origin of the PL features, we have performed empirical pseudopotential calculations for a range of In compositions with both the uniform and peaked profiles. The results are summarized under the heading "Model 1" in Table I. For all composition profiles tested, we find only a single bound electron state, while all six calculated hole states are bound. The calculated exciton energies E_x [see Eq. (5)], for the bound electron state lie between 1.29 and 1.34 eV, depending on composition. Thus the predicted optical properties of the Model 1 geometry are inconsistent with the observation of three PL peaks, and the predicted exciton energy is too high to account for the strong PL near 1.165 eV.

C. Second measurement of size and shape: Model 2

Further TEM observations were performed, this time in the $[0\bar{1}1]$ zone axis. The bottom of Fig. 3 shows a typical HRTEM image of one of the dots along $[0\bar{1}1]$. Although it is well established that HRTEM images show a contrast which is the result of overlapping of (a) structural contrast, (b) compositional contrast, and (c) strain contrast (consequently, it is extremely difficult to relate the contrast features with the actual shape of the dot without computer simulations), a careful analysis of the image, together with Fourier filtering, provides a clear picture of the In rich area. We thus obtain different structural data, namely, the height of the dots is 35 Å, the diameter of the base is about 200 Å, and the diameter of the top is 160 Å. The angle between the dot base and the dot side is 54°. The difference between these measurements and those of the previously described plan-view TEM image arise because the contrast image in the plan view does not correspond to the physical size of the dot itself, but rather to a mean strain field which is averaged across the thickness of the specimen. The improved resolution of HRTEM over the previous plan view TEM images is apparent from Fig. 3. Based on these improved measurements, we introduce a Model 2 geometry, shown in Fig. 1(b).

D. Pseudopotential calculations for Model 2 and comparison with experiment

We perform pseudopotential calculations for the geometry of Model 2, varying the In composition as before. Figure 5 shows the energies and wave functions of the hole states and electronic states for $\bar{x}_{\mathrm{In}}=60\%$ and a nonuniform composition

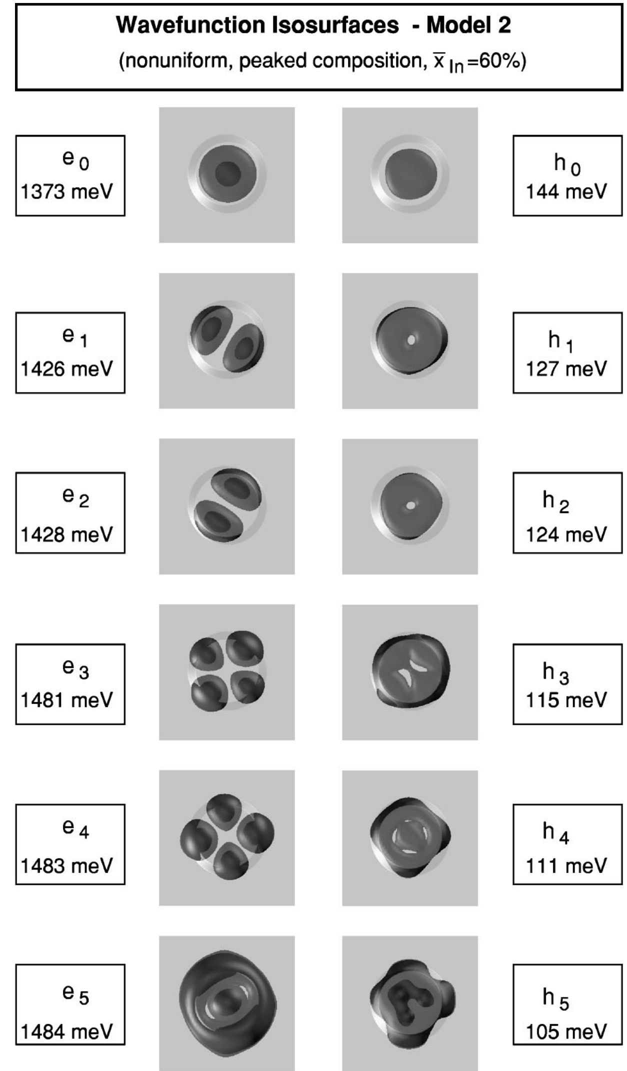

FIG. 5. Top view of envelope function isosurfaces containing 75% of the probability for the Model 2 dot geometry of Fig. 1(b) with nonuniform, peaked composition having average In content $\bar{x}_{\mathrm{in}}=60\%$. We give the single-particle energies ε measured relative to the GaAs VBM. All levels shown are localized to the dot.

profile. The wave-function images show isosurfaces of charge density containing 75% of the charge. The wetting layer is unchanged from Model 1, so the thresholds for the electrons and holes to become unbound from the dot are still $e_{\mathrm{WL}}=1493$ meV and $h_{\mathrm{WL}}=41.5$ meV, respectively. This time there are three dot-localized states, e_0, e_1, and e_2. Depending on the composition profile, states e_3, e_4, and e_5 can be either wetting layer states or localized to the dot. States e_3, e_4, and e_5 are dot localized when $\bar{x}_{\mathrm{In}}=60\%$, but combine with the wetting layer continuum when the In content is lower or the composition profile is uniform. As before, all calculated hole states are dot localized.

Table I gives the calculated exciton energies for Model 2 with different average In composition for both nonuniform and uniform profiles. We see that the closest match of experiment to theory is again for $\bar{x}_{\mathrm{In}}=60\%$ with a nonuniform, peaked composition (values are indicated by boldface char-

acters in Table I). These values are shown as bold arrows above the PL spectra in Fig. 2. This time the agreement with the PL data is much better: we find three exciton shells, and energies agree to within 30–40 meV. The calculated energies are consistently higher than the centers of the Gaussians fit to the PL. Part of this discrepancy is due to exchange and correlation effects between excitons in these highly excited dots (neglected in our calculations). Pseudopotential calculations with configuration interaction for multiexcitons in similar SK dots[48] predict redshifts between 5 and 30 meV due to multiexciton interactions.

From the calculated exciton energies predicted by our pseudopotential calculations, we attribute the experimental PL features to the following transitions: (i) the broad peak centered around 1.165 eV is identified as the e_0-h_0 (fundamental) exciton transition in the dots; (ii) the obscured peak near 1.25 eV is due to the e_1-h_1 and e_2-h_2 (secondary) exciton transitions. (iii) the third broad peak centered around 1.315 eV is identified as the third shell excitons (e_3-h_3, e_4-h_5, and e_5-h_4) and (iv) the double peak with energies 1.4 and 1.43 eV is associated with wetting layer transitions.

The polarization ratio $\lambda=P_{110}/P_{1\bar{1}0}$ of exciton peaks in polarized PL spectra has recently been used as an indicator of dot shape.[52] Although we have not performed polarized PL measurements for our samples, we can make predictions from our model. We have calculated the polarization ratio for the e_0-h_0 excitonic transition using our best geometry (Model 2) with $\bar{x}_{\mathrm{In}}=60\%$. For a uniform composition profile we find $\lambda=0.981$, and the anisotropy increases to $\lambda=0.966$ for the nonuniform, peaked composition profile. The $E_{e_1-h_1}$ and $E_{e_2-h_2}$ transitions are highly polarized, but are separated in energy by only 3 meV. The polarization ratio P_{100}/P_{010} for all transitions is essentially one, as required by C_{2v} symmetry and in agreement with measurements on other self-assembled dots.[52]

The intrinsic dipole moment of the exciton, given by the effective growth direction separation of the center of mass of the electron and hole states, has been cited as an indicator of composition profile. Although we have not performed linear Stark effect measurements to experimentally determine this quantity, we can give theoretical predictions from our model. For a uniform composition profile we find a small dipole moment $p_z=0.5e$ Å, with the hole *slightly above* the electron. For the peaked composition, the dipole moment is essentially unchanged, $p_z=0.4e$ Å (hole *above* electron).

We conclude that our alloy dot is best described by the Model 2 [Fig. 1(b)] geometry with a peaked composition having an average In content $\bar{x}_{\mathrm{In}}=60\%$ and a maximal concentration of $x_{\mathrm{max}}=80\%$. Our results for the excitonic energies (in eV) and corresponding polarization ratios λ and dipole moments p_z are

$$E_{e_0-h_0}=1.192;\quad \lambda=0.966;\quad p_z=0.3e\ \text{Å}$$

$$E_{e_1-h_1}=1.264;\quad \lambda=1.511;\quad p_z=0.2e\ \text{Å}$$

$$E_{e_2-h_2}=1.268;\quad \lambda=0.646;\quad p_z=0.4e\ \text{Å}$$

$$E_{e_3-h_3}=1.334;$$

$$E_{e_4-h_5}=1.345;$$

$$E_{e_5-h_4}=1.345. \tag{6}$$

V. THEORETICAL STUDY OF THE EFFECTS OF COMPOSITIONAL CHANGES ON ELECTRONIC PROPERTIES OF DOTS

Having established via experiment-theory interaction a reasonable size, shape, and compositional profile of these dots, we now turn to the study of the generic effects of In/Ga compositional variations on the dots' electronic properties. Composition variation has several interdependent effects: (i) band offsets are modified, exhibiting bowing as well as strain dependence; (ii) effective masses are modified by both composition and strain; and (iii) the strain fields themselves depend on the composition profile. Pseudopotential calculations treat all these effects, making them a good tool for studying compositional variations. We performed pseudopotential calculations for a dot with the final geometry of Model 2 [Fig. 1(b)] using (i) a range of In concentrations $\bar{x}_{\mathrm{In}}$ with a fixed uniform composition profile and (ii) the same range of $\bar{x}_{\mathrm{In}}$ with a nonuniform, peaked composition. From these calculations we are able to (i) compare strain energies for different composition profiles, (ii) present strain profiles and strain-modified confinement potentials illustrating the effect of composition variation on the dot's confinement properties, (iii) study the effects of varying the In concentration while keeping a fixed, uniform composition profile, and (iv) compare the electronic properties of a uniform vs nonuniform, peaked composition profile.

A. Strain energies for different composition profiles

Strain energy is believed to drive the In into a nonuniform profile within the dot.[16] We have observed such nonuniform In distribution in our EELS and EDX composition profiles. To see if the composition profiles are consistent with a strain-driven mechanism, we compare the total strain energy as calculated by VFF for dots with different composition profiles. We find that dots with the nonuniform, peaked composition profile do indeed have lower strain energy than dots with uniform compositions. However, for the model considered here, the decrease in total strain energy for the nonuniform dots is only about 0.5 meV/atom, which is too small to make the peaked profile thermodynamically favorable at realistic growth temperatures. From our strain calculations on embedded dots, we cannot comment on the role of surface strain on composition profiles during the growth of the InGaAs dots.

B. Strain profiles and confinement potentials

Using our relaxed atomic positions, we calculate strain fields from the distortion of the tetrahedron of nearest neighbors for each cation. We plot the strains in the top part of Fig. 6, for $\bar{x}_{\mathrm{In}}=60\%$ and both a uniform and nonuniform, peaked

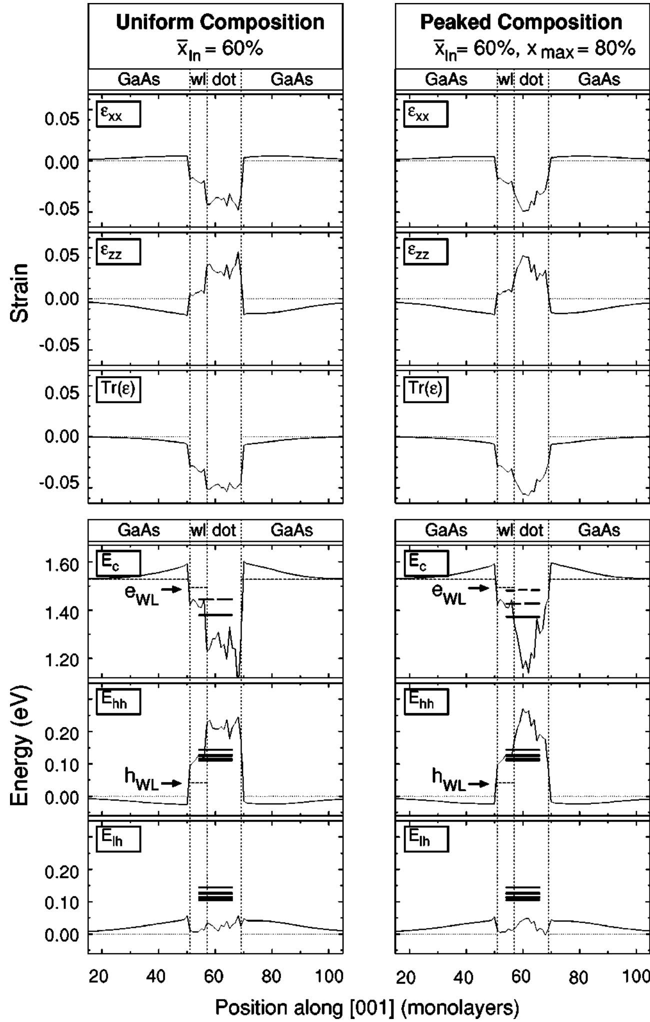

FIG. 6. Strain profiles (top) and confinement (bottom) for a dot with the geometry shown in Fig. 1(b). Left side of the figure shows results for a uniform In composition within the dot, and the right side is for nonuniform In composition, peaked in the center of the dot (as shown on the right side of Fig. 1). Strain perpendicular (ϵ_{xx}) and parallel (ϵ_{zz}) to the growth direction, and volume distortion (Tr ϵ) are shown. The small (<0.005), constant strain in ϵ_{xx} and ϵ_{zz} above and below the dot is due to the artificial interaction with periodic dot images in the growth direction of the calculation. Confinement potentials for conduction electrons (E_c), heavy holes (E_{hh}), and light holes (E_{lh}) are shown for illustrative purposes only and are not used in the pseudopotential method. Pseudopotential single-particle energies are shown as short lines in the confinement potential figures.

composition (shown on the left and right sides of the figure, respectively). The jagged features in the graphs arise from atomic scale material fluctuations in the random alloy. (Such alloy fluctuations are related to exciton localization in bulk films.[17,18]) For the figure we have averaged over 72 adjacent atoms in each monolayer to reduce the fluctuations. The figure shows the strain perpendicular (ϵ_{xx}) and parallel (ϵ_{zz}) to the growth direction as well as the volume distortion (Tr ϵ). Due to the periodic boundary conditions in our calculation, there is a small coupling between vertically stacked periodic images, causing an artificial, small (<0.005), constant strain in ϵ_{xx} and ϵ_{zz}. Otherwise, the strain fields decay away from the dot, as expected for a zero-dimensional structure. We see that both the wetting layer and the dot are epitaxially strained: there is compression in the growth plane ($\varepsilon_{xx}<0$) and expansion in the growth direction ($\varepsilon_{zz}>0$). The expansion in the growth direction is compensated for by compression in the GaAs above and below the dot. Strain is considerably stronger within the dot than in the wetting layer. This is consistent with the different average In compositions, 30 and 60%, for the wetting layer and dot, respectively. For the nonuniform, peaked distribution we see a peak in the strain corresponding to the peak in the In concentration.

To illustrate the effect of strain and composition on confinement properties, we have calculated the strain-modified confinement potentials using a simple $\mathbf{k}\cdot\mathbf{p}$ model describing the coupling of harmonic strain to the valence-band maximum and conduction-band minimum of cubic materials.[53] This approximation is not a necessary step to our calculations, since these modeled confinements never enter the pseudopotential calculations. Rather, the confinement potentials are a useful tool for giving a qualitative picture of the confinement mechanism. The confinement potentials for electrons, heavy holes, and light holes are shown in the bottom part of Fig. 6. The left side of the figure shows the confinement potential for uniform composition, and the right side of the figure shows the effects of a nonuniform, peaked In distribution on the confinement potential. Short lines in the dot layer indicate the pseudopotential calculated electron and hole energies and arrows denote the thresholds of the wetting layer continua for electrons and holes. From the graphs, we see that the confinement potentials resemble the strain fields for electrons and heavy holes, while the light hole potential is relatively flat. Due to the weak light hole confinement, we expect bound hole states to be predominately heavy hole in nature. The confinement of the electrons and heavy holes is much stronger in the dot than the wetting layer, and the dot with nonuniform, peaked composition has a peaked confinement potential, too. Thus we see a trend for stronger confinement with increasing In content (as a result of the smaller band gap of InAs, even in the presence of larger strain), and might expect our pseudopotential calculations to show stronger electron and heavy hole binding with either increasing In content or nonuniform, peaked compositions.

C. Pseudopotential results for uniform composition

Using the pseudopotential method, we have calculated single-particle energies, Coulomb matrix elements, and exciton energies for Model 2 dots with a uniform composition profile and $\bar{x}_{\rm In}=50$, 55, and 60%. Figure 7 shows the change in single-particle energies as the In content is increased but kept uniform. For the range of In concentration considered, the binding energy of electrons and holes increases nearly linearly with increasing In content. In going from $\bar{x}_{\rm In}=50\%$ to $\bar{x}_{\rm In}=60\%$, the electron energies change by about 35 meV, and the hole energies change by about 20 meV. Thus our expectation based on the strain-modified confinement potentials are born out.

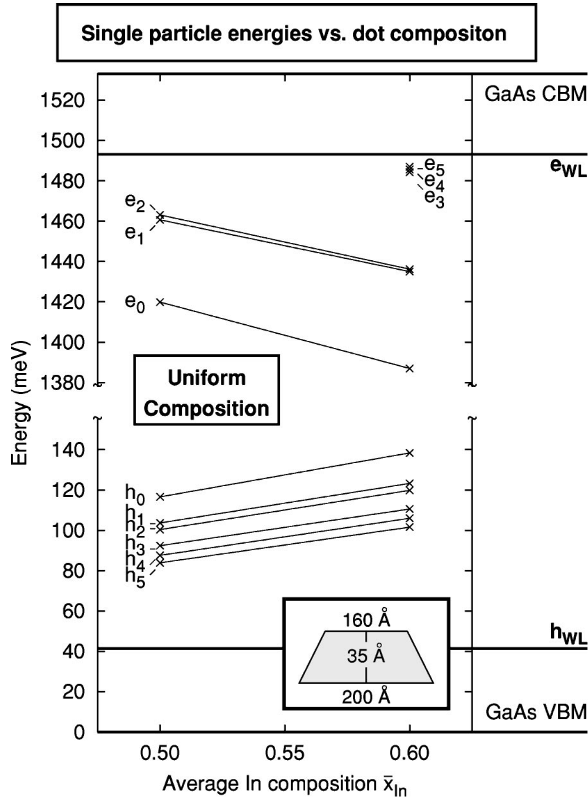

FIG. 7. Energy of the single-particle states vs average In concentration for the Model 2 geometry [Fig. 1(b)] with uniform $\bar{x}_{\mathrm{In}}$ In distribution.

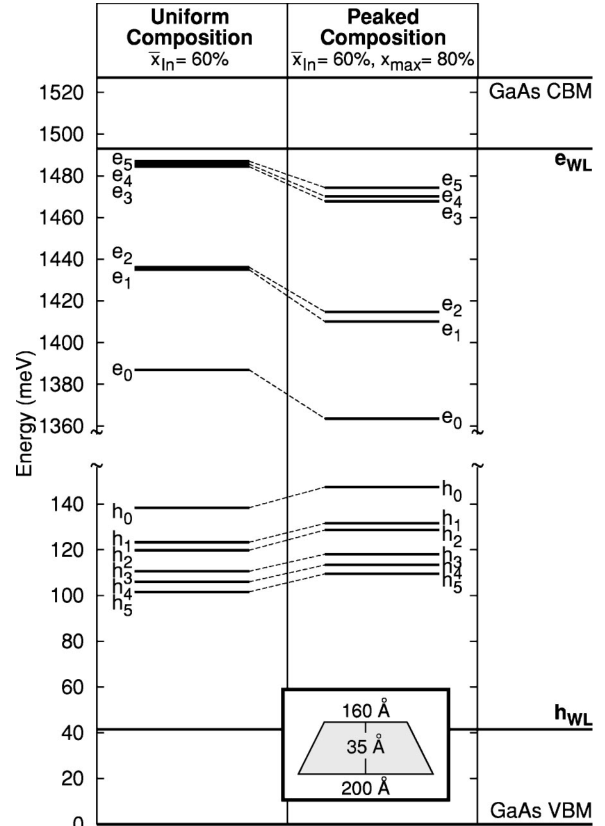

FIG. 8. Single-particle energy levels for two different composition profiles with the Model 2 geometry of Fig. 1(b). The "peaked composition" concentrates the In in the center of the dot (as shown on the right side of Fig. 1), and enhances the binding of electrons and holes to the dot.

Two mechanisms cause the exciton energy to be redshifted when the In content increases: (i) the electron and hole become more tightly bound to the dot, which decreases the difference in single-particle energies $\Delta\varepsilon$, and (ii) the smaller spatial extent of the electron and hole wave functions causes the attractive direct Coulomb energy J to increase. Numerical values for J, with resulting exciton energies $E_x = \Delta\varepsilon - J$, are shown in Table I. We see that reduction in $\Delta\varepsilon$ contributes more to the exaction redshift than the increasing direct Coulomb energy J. The fundamental exciton has a redshift of 90 meV when increasing In content from $\bar{x}_{\mathrm{In}} = 50\%$ to $\bar{x}_{\mathrm{In}} = 60\%$. The redshift of the excited exciton states is about a factor of 2 smaller.

D. Pseudopotential results for nonuniform composition

To study the effects of varying the spatial distribution of In, we have repeated pseudopotential calculations for average compositions $\bar{x}_{\mathrm{In}} = 50$, 55, and 60%. The single-particle energies are shown in Fig. 8 and the resulting exciton energies are listed in Table I. We see that the exciton energies are 15–30 meV lower for dots with peaked, nonuniform profiles as compared to the corresponding uniform dots. This is primarily due to the smaller energy gap between electron and hole levels, with only a small ~1-meV contribution from the enhanced Coulomb interaction due to the greater localization of the wave functions. As seen in Fig. 8, both electron and hole levels contribute to the decreased energy gap.

VI. CONCLUSION

By interactive iteration of theory and experiment we have arrived at a consistent picture of both the material and electronic structure of a sample of InGaAs/GaAs alloy dots. In our model with best experiment-theory agreement, we find a truncated conical shape, with height 35 Å, base diameter 200 Å, and top diameter 160 Å [Model 2 of Fig. 1(b)]. The In composition in our best model is nonuniform, starting at 30% at the base of the dot, reaching a maximum of around 80% at about one-third the dot height, and decreasing back to about 30% at the top of the dot, giving an average In composition $\bar{x}_{\mathrm{In}} = 60\%$. From EELS and TEM measurements, and a comparison of PL and pseudopotential calculations we have estimated the wetting layer far from the dot to be 4 ML's thick with 50% In content (thickness 12 Å). Near the dot, the wetting layer is depleted and broadened, which we model as 6 ML's with 30% In content.

Pseudopotential calculations on our best model structure find six dot-localized electron states and many dot-localized hole states. We have identified four features in the PL spectra (Fig. 2): (i) the broad peak around 1.165 eV is associated with the fundamental $e_0 - h_0$ exciton (calculated energy 1.192 eV); (ii) an obscured peak centered near 1.25 eV associated with the secondary excitons, $e_1 - h_1$ and $e_2 - h_2$ (calculated energies 1.264 and 1.268 eV); (iii) a broad peak

located near 1.315 eV associated with a third exciton shell e_3-h_3, e_4-h_5, and e_5-h_4 (calculated energies 1.334, 1.345, and 1.245 eV); and (iv) the double peak near 1.4 eV is associated with the wetting layer (the calculated exciton energy in 4 ML's of $In_{0.5}Ga_{0.5}As$ is 1.40 eV). Thus, for the iterated model geometry, we find that theoretical and experimental exciton energies agree to within $\lesssim 30$ meV. The majority of this difference may be attributed to multiexciton exchange and correlation interactions in the highly excited PL spectra,[48] which were not included in our calculations.

We find that by either increasing the amount of In within the dot or by concentrating a given amount of In near the center of the dot, both electrons and holes become more strongly bound to the dot. A small change of In content from 50 to 60% causes an exciton redshift of about 70 meV (Table I), due primarily to shifts in single-particle energies (Fig. 7). Changing the composition profile from a uniform In distribution to a centrally peaked distribution can redshift the exciton by an additional 20–40 meV (Table I), again due primarily to shifts in single-particle energies (Fig. 8).

Thus we have found an interactive iteration of theory and experiment to be capable of determining both the material and electronic structure of self-assembled dots. The experimental techniques of PL spectroscopy, HRTEM, EELS, and EDX and theoretical pseudopotential techniques are sensitive to the composition details of nanostructures. The results presented here highlight the sensitivity of electronic structure to the material structure and the importance of accurate measurements of dot size, shape, and material composition.

ACKNOWLEDGMENTS

Work at NREL was supported by the DOE Office of Science – Basic Energy Sciences, Division of Materials Sciences under Contract No. DE-AC36-99GO10337. Work at Lecce was partially supported by PRA-INFM and EC through SQUID.

[1] A. Zunger, MRS Bull. **23**, 35 (1998).
[2] L.-W. Wang and A. Zunger, Phys. Rev. B **59**, 15 806 (1999).
[3] H. Fu, L.-W. Wang, and A. Zunger, Phys. Rev. B **57**, 9971 (1999).
[4] C. Pryor, J. Kim, A.J. Williamson, and A. Zunger, J. Appl. Phys. **83**, 2548 (1998).
[5] A.J. Williamson, A. Zunger, and A. Canning, Phys. Rev. B **57**, R4253 (1998).
[6] A.J. Williamson, A. Franceschetti, H. Fu, L.W. Wang, and A. Zunger, J. Electron. Mater. **28**, 414 (1999).
[7] A. Franceschetti and A. Zunger, Phys. Rev. Lett. **78**, 915 (1997).
[8] L.-W. Wang and A. Zunger, Phys. Rev. Lett. **73**, 1039 (1994).
[9] R. Leon, Y. Kim, C. Jagadish, M. Gal, J. Zou, and D.J.H. Cockayne, Appl. Phys. Lett. **69**, 1888 (1996).
[10] C. Lobo, R. Leon, S. Fafard, and P.G. Piva, Appl. Phys. Lett. **72**, 2850 (1998).
[11] P.B. Joyce, T.J. Krzyzewski, C.G. Bell, B.A. Joyce, and T.S. Jones, Phys. Rev. B **58**, R15 981 (1998).
[12] I. Kegel, T.H. Metzger, A. Lorke, J. Peisl, J. Stangl, G. Bauer, J.M. García, and P.M. Petroff, Phys. Rev. Lett. **85**, 1694 (2000).
[13] I. Kegel, T.H. Metzger, A. Lorke, J. Peisl, J. Stangl, G. Bauer, K. Nordlund, W.V. Schoenfeld, and P.M. Petroff, Phys. Rev. B **63**, 035318 (2001).
[14] X.Z. Liao, J. Zou, D.J.H. Cockayne, R. Leon, and C. Lobo, Phys. Rev. Lett. **82**, 5148 (1999).
[15] A. Krost, J. Bläsing, F. Heinrichsdorff, and D. Bimberg, Appl. Phys. Lett. **75**, 2957 (1999).
[16] N. Liu, J. Tersoff, O. Baklenov, A.L. Holmes, Jr., and C.K. Shih, Phys. Rev. Lett. **84**, 334 (2000).
[17] L.-W. Wang, L. Bellaiche, S.-H. Wei, and A. Zunger, Phys. Rev. Lett. **80**, 4725 (1998).
[18] S. Permogorov and A. Reznitsky, J. Lumin. **52**, 201 (1992).
[19] J. Kim, L.-W. Wang, and A. Zunger, Phys. Rev. B **57**, R9408 (1998).
[20] L.-W. Wang, J. Kim, and A. Zunger, Phys. Rev. B **59**, 5678 (1995).
[21] A.J. Williamson, L.W. Wang, and A. Zunger, Phys. Rev. B **62**, 12 963 (2000).
[22] L.-W. Wang and A. Zunger, J. Phys. Chem. **100**, 2394 (1994).
[23] J.A. Barker and E.P. O'Reilly, Phys. Rev. B **61**, 13 840 (2000).
[24] J.-Y. Marzin, J.-M. Gérard, A. Izraël, D. Barrier, and G. Bastard, Phys. Rev. Lett. **73**, 716 (1994).
[25] A. Wojs, P. Hawrylak, S. Fafard, and L. Jacak, Phys. Rev. B **54**, 5604 (1996).
[26] L. Jacak, A. Wójs, and P. Harylack, *Quantum Dots* (Springer-Verlag, Berlin, 1998).
[27] E. Dekel, D. Gershoni, E. Ehrenfreund, D. Spektor, J.M. García, and P.M. Petroff, Phys. Rev. Lett. **80**, 4991 (1998).
[28] L.R.C. Fonseca, J.L. Jimenez, J.P. Leburton, and R.M. Martin, Phys. Rev. B **57**, 4017 (1998).
[29] N.A. Bruce and P.A. Maksym, Phys. Rev. B **61**, 4718 (2000).
[30] P.W. Fry, I.E. Itskevich, D.J. Mowbray, M.S. Skolnick, J.J. Finley, J.A. Barker, E.P. O'Reilly, L.R. Wilson, I.A. Larkin, P.A. Maksym, M. Hopkinson, M. Al-Khafaji, J.P.R. David, A.G. Cullis, G. Hill, and J.C. Clark, Phys. Rev. Lett. **84**, 733 (2000).
[31] I.E. Itskevich, S.I. Rybchenko, I.I. Tartakovskii, S.T. Stoddart, A. Levin, P.C. Main, L. Eaves, M. Henini, and S. Parnell, Appl. Phys. Lett. **76**, 3932 (2000).
[32] M. Grundmann, O. Stier, and D. Bimberg, Phys. Rev. B **52**, 11 969 (1995).
[33] O. Stier, M. Grundmann, and D. Bimberg, Phys. Rev. B **59**, 5688 (1999).
[34] C. Pryor, Phys. Rev. B **57**, 7190 (1998).
[35] C. Pryor, Phys. Rev. B **60**, 2869 (1999).
[36] L.W. Wang, A.J. Williamson, A. Zunger, H. Jiang, and J. Singh, Appl. Phys. Lett. **76**, 339 (2000).
[37] J.M. García, G. Medeiros-Ribeiro, K. Schmidt, T. Ngo, J.L. Feng, A. Lorke, J. Kotthaus, and P.M. Petroff, Appl. Phys. Lett. **71**, 2014 (1997).
[38] R. Leon, S. Fafard, P.G. Piva, S. Ruvimov, and Z. Liliental-Weber, Phys. Rev. B **58**, R4262 (1998).

[39] S. Malik, C. Roberts, R. Murray, and M. Pate, Appl. Phys. Lett. **71**, 1987 (1997).

[40] S.J. Xu, X.C. Wang, S.J. Chua, C.H. Wang, W.J. Fan, J. Jiang, and X.G. Xie, Appl. Phys. Lett. **72**, 3335 (1998).

[41] S. Fafard and C.N. Allen, Appl. Phys. Lett. **75**, 2374 (1999).

[42] B. Lita, R.S. Goldman, J.D. Phillips, and P.K. Bhattacharya, Appl. Phys. Lett. **75**, 2797 (1999).

[43] R. Leon, D.R.M. Williams, J. Krueger, E.R. Weber, and M.R. Melloch, Phys. Rev. B **56**, R4336 (1997).

[44] N. Perret, D. Morris, L. Franchomme-Fossé, R. Côté, S. Fafard, V. Aimez, and J. Beauvais, Phys. Rev. B **62**, 5092 (2000).

[45] M. DeGiorgi, A. Vasanelli, R. Rinaldi, M. Anni, M. Lomascolo, S. Antonaci, A. Passeseo, R. Cingolani, A. Taurino, M. Catalno, and E. DiFabrizio, Micron **31**, 245 (2000).

[46] Note that standard envelope function calculations of the wetting layers make a number of approximationa, not shared by pseudopotential methods, e.g., the virtual crystal approximations, use of harmonic elasticity even for large lattice mismatches, and approximate electron-hole Coulomb energies. These differences lead to different electronic structure. A comparison of eight band $\mathbf{k}\cdot\mathbf{p}$ and pseudopotential calculations for quantum wells superlattices is given by D.M. Wood and A. Zunger, Phys. Rev. B **53**, 7949 (1996), showing that for $\lesssim$4-ML thick structures the errors of $\mathbf{k}\cdot\mathbf{p}$ are indeed significant.

[47] A. Franceschetti, H. Fu, L.W. Wang, and A. Zunger, Phys. Rev. B **60**, 1819 (1999).

[48] A.J. Williamson, A. Franceschetti, and A. Zunger, Europhys. Lett. **53**, 59 (2001).

[49] P.N. Keating, Phys. Rev. **145**, 637 (1966).

[50] R.M. Martin, Phys. Rev. B **1**, 4005 (1970).

[51] A. Silverman, A. Zunger, R. Kalish, and J. Adler, Phys. Rev. B **51**, 10 795 (1995).

[52] W. Yang, H. Lee, T.J. Johnson, P.C. Sercel, and A.G. Norman, Phys. Rev. B **61**, 2784 (2000).

[53] S.-H. Wei and A. Zunger, Phys. Rev. B **49**, 14 337 (1994).